PHYSICAL SCIENCES

Planar defect–free pure red perovskite light-emitting diodes via metastable phase crystallization

Yong-Hui Song[1,2]†, Jing Ge[1,3]†, Li-Bo Mao[1], Kun-Hua Wang[1], Xiao-Lin Tai[1], Qian Zhang[1,2], Le Tang[3], Jing-Ming Hao[1,2], Ji-Song Yao[1,2], Jing-Jing Wang[1,2], Tao Ma[1], Jun-Nan Yang[2], Yi-Feng Lan[2], Xue-Chen Ru[1], Li-Zhe Feng[1], Guozhen Zhang[1]*, Yue Lin[1]*, Qun Zhang[1,3,4]*, Hong-Bin Yao[1,2]*

Solution-processable all-inorganic CsPbI$_{3−x}$Br$_x$ perovskite holds great potential for pure red light-emitting diodes. However, the widely existing defects in this mixed halide perovskite markedly limit the efficiency and stability of present light-emitting diode devices. We here identify that intragrain Ruddlesden-Popper planar defects are primary forms of such defects in the CsPbI$_{3−x}$Br$_x$ thin film owing to the lattice strain caused by inhomogeneous halogen ion distribution. To eliminate these defects, we develop a stepwise metastable phase crystallization strategy to minimize the CsPbI$_{3−x}$Br$_x$ perovskite lattice strain, which brings planar defect–free CsPbI$_{3−x}$Br$_x$ thin film with improved radiative recombination, narrowed emission band, and enhanced spectral stability. Using these high-quality thin films, we fabricate spectrally stable pure red perovskite light-emitting diodes, showing 17.8% external quantum efficiency and 9000 candela meter^{-2} brightness with color coordinates required by Rec. 2020.

INTRODUCTION

Solution-processable metal halide perovskite (MHP) thin film is a promising emissive layer for next-generation light-emitting diodes (LEDs) due to high color purity, wide color gamut, and cost-efficiency (1–7). However, the rapid and uncontrollable crystallization of the MHP from precursor solution is prone to generating many defects in the formed thin films (8–11), which have been deemed the main cause of low luminescence efficiency, poor stability, and limited performance of the fabricated LEDs (12). In recently reported MHP LEDs, small-molecular additives have been used to guide the nonclassical crystallization process of the MHP, which involves the perovskite cluster nucleation, aggregation, and assembly to form surface-passivated and highly luminescent micro-/nanocrystalline thin films (13, 14); therefore, such a treatment has pushed the recorded external quantum efficiencies (EQEs) of MHP LEDs beyond 20% in both green (13, 15–18) and near-infrared (14, 19–21) regions.

However, the EQEs of vital pure red LEDs based on all-inorganic mixed halide CsPbI$_{3−x}$Br$_x$ perovskite with high carrier mobility and color purity (1) are still low despite that similar small-molecular additive engineering has been tried in guiding the nonclassical crystallization of all-inorganic mixed halide CsPbI$_{3−x}$Br$_x$ perovskite (22–26). In such a mixed halide perovskite thin film, the planar defects as higher-dimensional lattice defects are predicted to be more inclined to form at the grain boundary and the intragrain in comparison to the single-halide perovskite system during the perovskite cluster assembly process, owing to much intensive distortion of the mixed halide lattice in the case of inhomogeneous halogen distribution, which heavily restricts the mixed halide perovskite device

efficiency and stability (8, 27, 28). Nevertheless, the experimental observation and exploration of these planar defects in the solution-processed CsPbI$_{3−x}$Br$_x$ thin film have not been reported, let along developing strategies to eliminate these defects for improving the performance of pure red CsPbI$_{3−x}$Br$_x$ perovskite LEDs.

Here, we use low-dose spherical aberration transmission electron microscope to identify the existence of Ruddlesden-Popper (RP) planar defects in the CsPbI$_{3−x}$Br$_x$ thin film and confirm that the formation of RP planar defects is related to the lattice strain induced by inhomogeneous halogen. To eliminate these defects, we further develop a metastable phase crystallization (MPC) strategy to homogenize the halogen distribution in CsPbI$_{3−x}$Br$_x$ thin films for achieving efficient and stable pure red LEDs. Our proposed MPC strategy consists of a reorganization step of a metastable precursor and a crystallization step of the metastable phase, which is featured by precise control of the additive compositions (forming metastable phase) and annealing process (initiating crystallization of metastable phase) to fabricate planar defect–free CsPbI$_{3−x}$Br$_x$ thin films. The resulting planar defect–free CsPbI$_{3−x}$Br$_x$ thin films perform improved radiative recombination and enable spectrally stable pure red perovskite LEDs with 17.8% EQE and a brightness of 9000 cd m^{-2}.

RESULTS

Nonclassical crystallization of CsPbI$_{3−x}$Br$_x$ thin film

In a typical nonclassical crystallization process of CsPbI$_{3−x}$Br$_x$ thin film, the mixed halide precursor experiences cluster nucleation, aggregation, and assembly steps to induce the crystallization of mixed halide CsPbI$_{3−x}$Br$_x$ perovskite (Fig. 1A). During this normal nonclassical mixed halide perovskite crystallization process, the inhomogeneous halogen distribution is initiated at the cluster nucleation and aggregation steps, which directly induces the formation of planar defects at the assembly and crystallization step due to the lattice strain among those nonuniform CsPbI$_{3−x}$Br$_x$ subunits. To make homogeneous halogen distribution in the CsPbI$_{3−x}$Br$_x$ perovskite, we proposed an MPC consisting of a reorganization step of a metastable precursor and a crystallization step of the metastable phase, which

[1]Hefei National Research Center for Physical Sciences at the Microscale, University of Science and Technology of China, Hefei, Anhui 230026, China. [2]Department of Applied Chemistry, University of Science and Technology of China, Hefei, Anhui 230026, China. [3]Department of Chemical Physics, University of Science and Technology of China, Hefei, Anhui 230026, China. [4]Hefei National Laboratory, University of Science and Technology of China, Hefei, Anhui 230088, China.
*Corresponding author. Email: yhb@ustc.edu.cn (H.-B.Y.); qunzh@ustc.edu.cn (Q.Z.); linyue@ustc.edu.cn (Y.L.); guozhen@ustc.edu.cn (G.Z.)
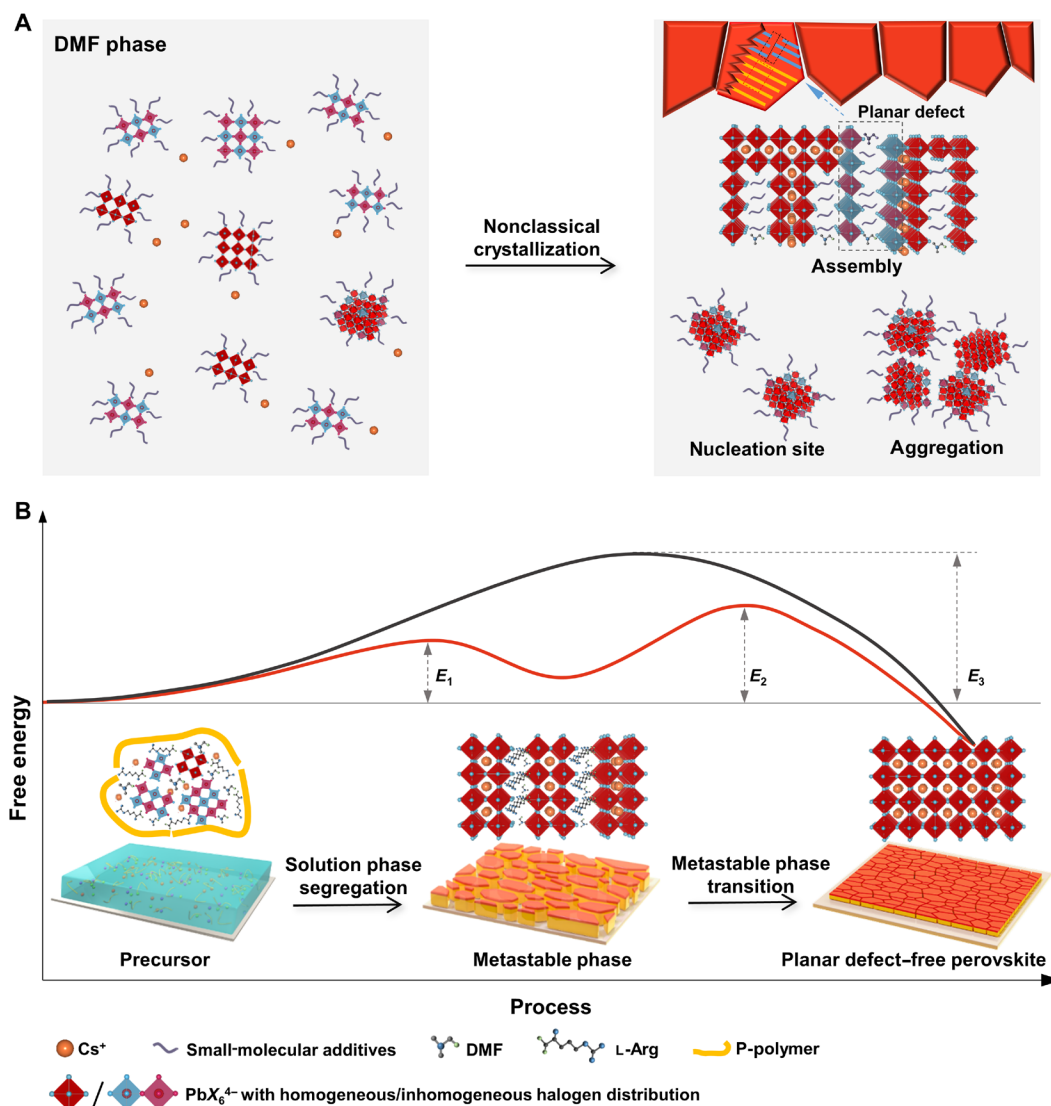†These authors contributed equally to this work.

Fig. 1. Schematic illustration of MHP crystallization process and the proposed different crystallization pathways. (**A**) Nonclassical crystallization process of small-molecular additives in mixed halide CsPbI$_{3-x}$Br$_x$ perovskite precursor solution and the crystalline phase formation with planar defects. (**B**) Illustration of free energy–dependent mixed halide CsPbI$_{3-x}$Br$_x$ crystallization process in two different pathways. The consecutive two-step low-energy barrier (E_1 and E_2) pathway involves the proposed metastable intermediate phase crystallization process. The high-energy barrier (E_3) pathway is a conventional one-step crystallization (OSC) process of MHP thin film. The crystal structure models reflect the corresponding interactions among L-arginine (L-Arg), poly(vinylidene fluoride-*co*-hexafluoropropylene) (P-polymer), and perovskite units for the well-controlled MPC crystallization process.

is featured by precise control of the additive compositions (forming metastable phase) and annealing process (initiating crystallization of metastable phase).

In detail, using the MPC strategy, we can guide the CsPbI$_{3-x}$Br$_x$ perovskite crystallization in a designated two-step fashion as shown in Fig. 1B: (i) A metastable intermediate phase is formed under the attachment effect of L-arginine (L-Arg) and phase segregation effect of poly(vinylidene fluoride-*co*-hexafluoropropylene) (PVDF-HFP; P-polymer) to make homogeneously mixed halide intermediate gel film with a lower-energy barrier (E_1) at a lower annealing temperature; (ii) the metastable intermediate phase with homogeneous halogen distribution completely transforms into a stable and planar defect–free perovskite thin film with a slightly higher-energy barrier (E_2), releasing out the L-Arg from the inside lattices of metastable

phase via a higher temperature annealing process. Compared to the traditional one-step crystallization (OSC) over the high-energy barrier (E_3) at a higher annealing temperature of CsPbI$_{3-x}$Br$_x$ thin film, the MPC strategy allows the film formation process to pass through a metastable intermediate phase transformation step with homogenizing halogen distribution, which is vital for planar defect–free perovskite crystallization.

Defect characterization and identification of different CsPbI$_{3-x}$Br$_x$ thin films

We first fabricated and characterized the CsPbI$_{3-x}$Br$_x$ thin film without any additives to reveal its crystallinity and defects. The results indicate a very low crystallinity of the obtained thin film and the wide presence of many types of defects including point defects

and planar defects in the crystal domains (fig. S1), implying that the high-quality crystallization of mixed halide $CsPbI_{3-x}Br_x$ thin film needs careful implementation. We then carried out precise control of the additive compositions and annealing process for MPC of $CsPbI_{3-x}Br_x$ thin film and compared it with the films treated by no P-polymer–induced phase segregation (NPS) crystallization and OSC, respectively (more information in Materials and Methods).

We used transmission electron microscopy (TEM) to investigate the nanostructures and identify the defects of the obtained $CsPbI_{3-x}Br_x$ thin films. All thin films exhibit typical polycrystalline characteristics containing nanocrystalline domains and abundant grain boundaries (Fig. 2, A to C). The lateral sizes of these nanocrystalline domains are around tens of nanometers, and the size distribution in the $CsPbI_{3-x}Br_x$ thin film obtained by MPC shows the best uniformity with the largest surface coverage (fig. S2). The high-resolution TEM (HRTEM) images show that there are many intragrain planar defects and grain boundary defects in both NPS (fig. S3) and OSC films (fig. S4), indicating the widespread existence of planar defects in these $CsPbI_{3-x}Br_x$ thin films without carefully controlled crystallization. The high-angle annular dark-field scanning TEM (HAADF-STEM) images further show that the intragrain planar defects propagate along the (100) and (010) planes throughout the nanocrystalline domains and display maze-like patterns in the NPS and OSC thin films (Fig. 2, D and E). In contrast, the nanocrystalline domain of MPC thin film shows intact crystal structure without any intragrain planar defects (Fig. 2F). The highly oriented attachment of the nanocrystalline domains without apparent grain boundary defects in MPC thin film (fig. S5) is very similar to the grain boundary of the aragonite nanoplatelets in the nacre (29), indicating the precise control of the film formation via MPC.

Furthermore, we observed two cesium halide layers with rock salt stacking at the two side edges of the planar defects, based on which these planar defects can be identified as RP planar faults (Fig. 2, G and H). The atoms around the RP planar defects in the NPS and OSC films exhibit an irregular arrangement featuring a large lattice mismatch with much intensive lattice strain in the thin film (figs. S6, S7, and S9). Moreover, the interconnection of the RP defects inside the grain of NPS and OSC yields typical rectangular regions restricted by the defect, especially for the much more lattice-mismatched NPS film (fig. S10, A and B). In contrast, the MPC film exhibits a relatively low lattice-strained atomic arrangement (Fig. 2I and figs. S8 and S9), and the specific atomic assignment also confirms that there is much more uniform distribution of I and Br in the lattice of the MPC film in comparison to that of the NPS and OSC films (fig. S10, D to F). On the basis of the above results, we speculated that the MPC process can promote the maximized mixing of halogen ions in the formed thin film for minimizing the lattice strain to avoid the formation of intragrain RP planar defects.

MPC mechanism for RP planar defect–free $CsPbI_{3-x}Br_x$ thin film
We further interpreted the mechanism by which the L-Arg and P-polymer participated in the formation of the metastable intermediate phase for planar defect–free crystallization. We used atomic force microscopy (AFM) to reveal the morphology evolution under the lower-temperature annealing at 90°C (Fig. 3). A continuous liquid-liquid phase segregation process in which the large domains that gradually divided into smoother and small domains were observed in the MPC thin film (Fig. 3, A to C), which can be attributed to the behavior of the phase segregation induced by the wrapping

effect of P-polymer in the precursor (fig. S11). In contrast, in the same annealing process at 90°C, there was no phase segregation phenomenon in the NPS film (Fig. 3, D to F), indicating that the addition of P-polymer is indispensable for MPC. Moreover, the residual N,N'-dimethylformamide (DMF) solvent content measurement (fig. S12) confirmed that the DMF content in MPC film was much higher than that in NPS film during the low-temperature annealing process, indicating that P-polymer played a vital role in wrapping the DMF solvent inside to promote the formation of metastable intermediate phase. The metastable phase system with more DMF residual solvent enables the mesocrystalline mixed halide phase, having sufficient conditions to obtain a large degree of freedom, which promotes the more uniform distribution of I and Br ions in the precursor thin film and facilitates the following complete transformation into planar defect–free perovskite. This metastable phase is vital for the MPC as unraveled in biomineralization that the presence of dense metastable precursors triggers the initial nucleation of well-ordered biomineral crystallites (30, 31). As for the OSC film, the phase segregation process might be too fast to be observed (Fig. 3, G to I) due to its rapid crystallization at high-temperature annealing state.

The phase segregation in our MPC precursor thin film triggered the metastable intermediate phase formation for the subsequent planar defect–free crystallization. We performed the HRTEM characterizations to show the metastable intermediate phase structure (fig. S13), indicating the appearance of the mesocrystalline structure in the metastable intermediate phase after annealing at 90°C due to the strong hydrogen bonding interaction between the guanidine group of L-Arg and the perovskite precursor (fig. S14). The x-ray diffraction (XRD) analysis further confirmed that the mesocrystalline structure appeared in the MPC precursor thin film at the lower-temperature (90°C) annealing state and then totally transformed into a three-dimensional (3D) perovskite structure after higher-temperature (120°C) annealing (fig. S15, A and B). Moreover, the ex situ photoluminescence (PL) measurement was performed to explore the luminance efficiency evolution of the MPC film during the crystallization process (fig. S16). Accompanying the transformation of the MPC film from the low-dimensional metastable phase to 3D perovskite phase, the PL quantum yield (PLQY) of the MPC film increases, the full width at half maximum (FWHM) of the PL peak decreases, and the PL peak position gradually red shifts and lastly locates at 638 nm. The transformation of the MPC film from low- to high-temperature annealing states was also revealed by the AFM (fig. S17), showing that, when the annealing temperature was increased to 120°C, the phase separation process was still going on slowly and the lateral grains increased as well promoting the MPC film to be more smoothed with uniform grain size distribution. In contrast, although mesocrystalline structures were observed in the NPS film, most of them still existed in the film after the final annealing process (fig. S15, C and D), indicating that they are not the metastable phases in the NPS film, probably due to the less content of DMF solvent in comparison to MPC film (fig. S12). For the OSC film with rapid crystallization, mesocrystalline structures were even not observed during the annealing process (fig. S15, E and F). Therefore, the addition of P-polymer along with the well-controlled annealing process is vital for the homogenous halogen reorganization in metastable intermediate phase (fig. S18), leading to intragrain and grain boundary defect-free mixed halide $CsPbI_{3-x}Br_x$ thin film with low surface roughness (fig. S19). To confirm that the L-Arg remains in the final MPC thin film, we performed the energy-dispersive x-ray spectroscopy
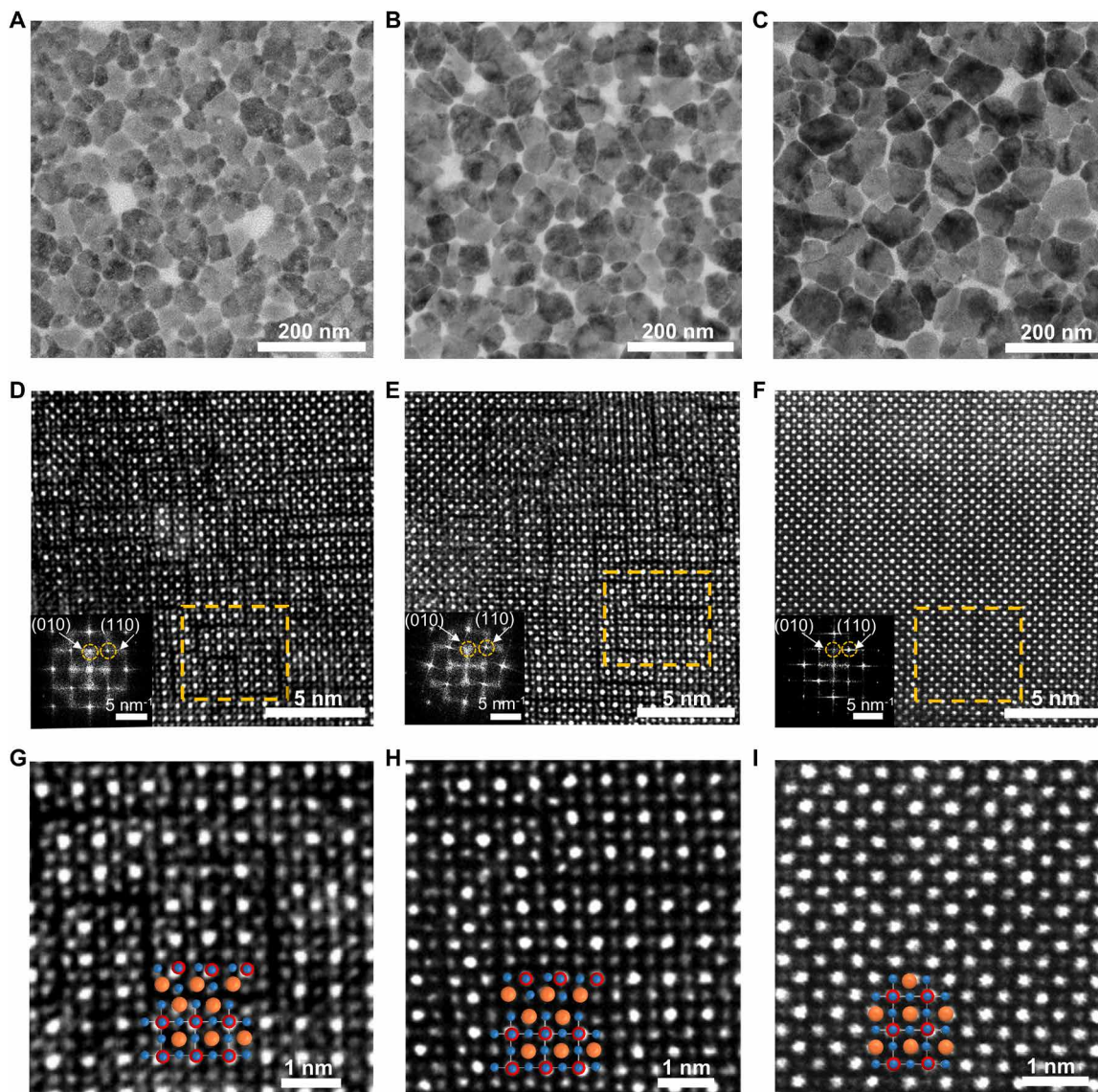
Fig. 2. TEM and atomic resolution HAADF-STEM images of CsPbI$_{3-x}$Br$_x$ thin film obtained with different crystallization progress. (**A** to **C**) Bright TEM images of no P-polymer–induced phase segregation (NPS) (A), OSC (B), and MPC (C) thin films showing the polycrystalline characteristics composed of nanocrystalline domains. (**D** to **F**) HAADF-STEM images of the NPS (D), OSC (E), and MPC (F) intergrain domains. Insets are the corresponding fast Fourier transform (FFT) patterns. Planar defects are observed in NPS and OSC nanocrystalline domains, and no planar defect exists in MPC nanocrystalline domain. (**G** to **I**) Atomic resolution HAADF-STEM images of the corresponding square area denoted in (D) to (F). The atomic structures are presented to identify the planar RP defects in the NPS and OSC thin film. Colors of the balls represent the following: orange, cesium; red, lead; and blue, halide.

(EDS) mapping and XPS analysis on MPC thin film and CsPbI$_{3-x}$Br$_x$ thin film without L-Arg. The results show the presence of the N element that is derived from L-Arg in the MPC thin film, indicating that L-Arg is eventually distributed among the grain boundaries or on the grain surfaces of the MPC thin film (fig. S20).

Optoelectronic properties of the CsPbI$_{3-x}$Br$_x$ thin films

To study the impact of RP defects on the energy band of CsPbI$_{3-x}$Br$_x$, we conducted the density-of-states (DOS) analysis using first-principles calculations. On the basis of the atomic resolution HAADF-STEM images (Fig. 2, G to I), we built three different types of lattice models including defect-free, internal 1D RP defect, and 2D RP defect confinements to represent MPC, OSC, and NPS films, respectively

(Fig. 4A and figs. S21 and S22). Compared to the defect-free model, the existence of 1D RP defects slightly increases the intrinsic bandgap of the CsPbI$_{3-x}$Br$_x$ and introduces a trap-like state isolating at the edge of valance band maximum (fig. S21). As the 1D RP defect turns to 2D, the trap state retains and the intrinsic bandgap increases by more than 0.3 eV (Fig. 4, B and C, and fig. S22). Such an increase in bandgap is attributed to the quantum confinement effect as the defect-induced isolated region size is below the Bohr radius of CsPbI$_{3-x}$Br$_x$ perovskite (*32*, *33*).

To elucidate the influence of energy band change on the optical properties of CsPbI$_{3-x}$Br$_x$ thin films, we performed femtosecond time-resolved transient absorption (fs-TA) spectroscopy. Right after the optical excitation, the photoinduced bleaching (PB) and photoinduced
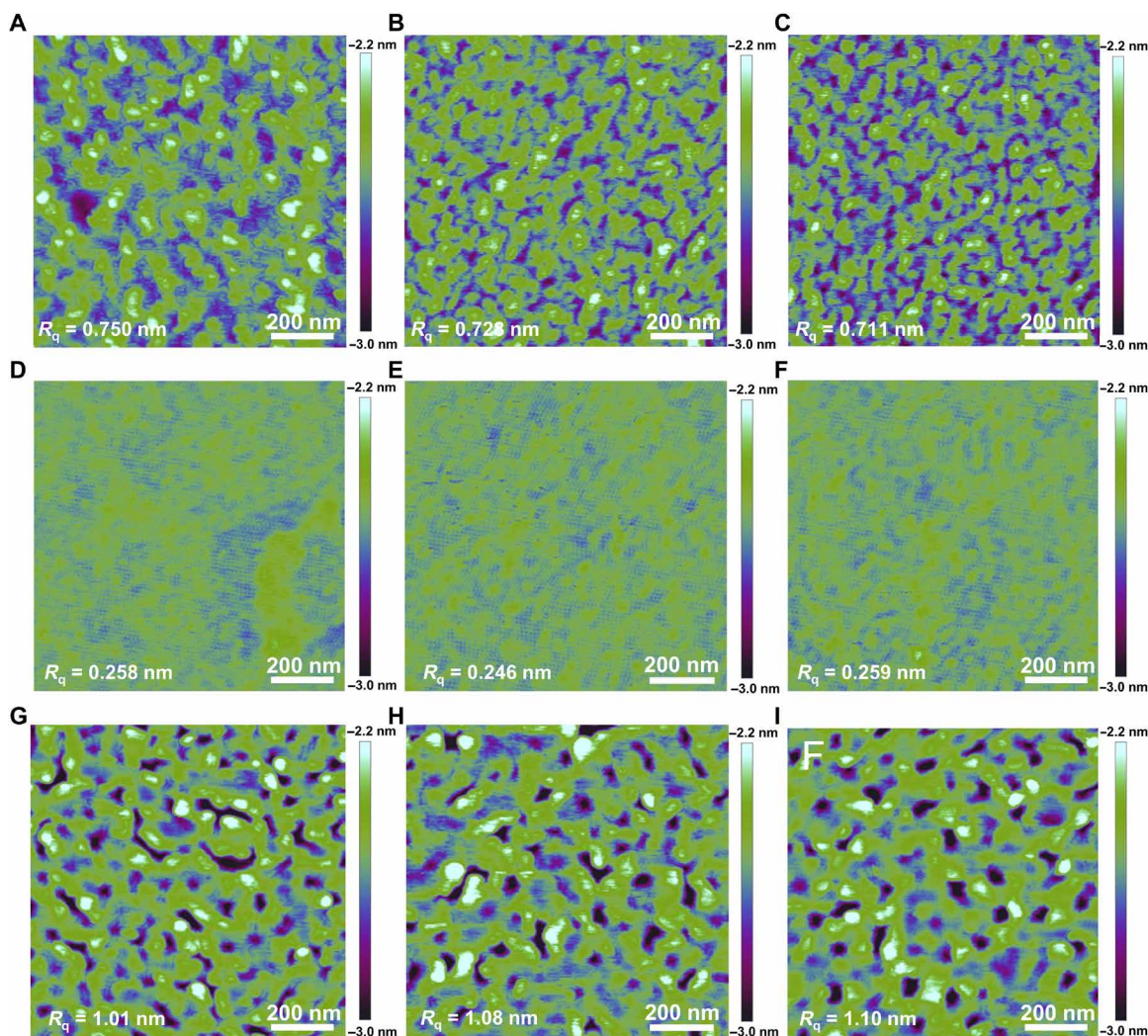
Fig. 3. AFM analysis of morphology variation to show the phase segregation of perovskite precursor thin film during annealing. (**A** to **C**) AFM image with surface roughness of the MPC film annealing at 90°C for 2, 5, and 10 min, respectively. R_q, roughness of root mean square. (**D** to **F**) AFM image with surface roughness of the NPS film annealing at 90°C for 2, 5, and 10 min, respectively. (**G** to **I**) AFM image with surface roughness of the OSC film annealing at 110°C for 2, 5, and 10 min, respectively. R_q represents the roughness of root mean square.

absorption (PA) features, corresponding to negative and positive signals, respectively, appear instantaneously around the exciton resonances (Fig. 4, D to F). The broadband PA feature at the red side can be associated with the presence of nonequilibrium hot carriers in the system. Thus, the carrier screening effect leads to renormalization of the bandgap (34). After the hot carriers relax down to the band edge (>1.5 ps) to form excitons, robust exciton-exciton interactions give rise to the PA feature at the blue side due to the blue shift of exciton energy, while the PB feature dominates the fs-TA spectra due to the state-filling effect rather than stimulated emission, because the absorption excitonic peak matches the PB peak better than the emission peak of the perovskite thin films (fig. S23). The PB peak of NPS film shows a blue shift of more than 30 nm and a relatively large broadening compared to the MPC and OSC films owing to the much smaller size and nonuniform size distribution of 2D PR defect confinement-induced multiple bandgap in the NPS film (fig. S24). Notably, the MPC film exhibits a narrowest PB peak,

arising as a result of its pristine bulk phase without defect-restricted regions, which is commensurate with the observation of its narrowest PL emission profile (Fig. 4G). We also performed the time-correlated single-photon counting (TCSPC) measurements to examine the effect of planar defects on the radiative recombination process (fig. S25 and table S1). The MPC film presents the longest PL decay lifetime of 100 ns compared to the OSC (86 ns) and NPS (34 ns) films, indicating that proper crystallization control can eliminate the exciton capturing at the planar defects and thus leads to much improved PLQY. The MPC film exhibits the highest PLQY of 45% compared to the NPS (22%) and OSC (29%) films (Fig. 4G). In addition, the defect densities of the obtained thin films were measured by the space charge–limited current (SCLC) technique (Fig. 4, H and I, and table S2). The calculated densities of defect states associated with the electrons and holes inside the MPC film are 4.87×10^{15} and 3.46×10^{15} cm^{-3}, respectively, both of which are much lower than those of NPS and OSC films.
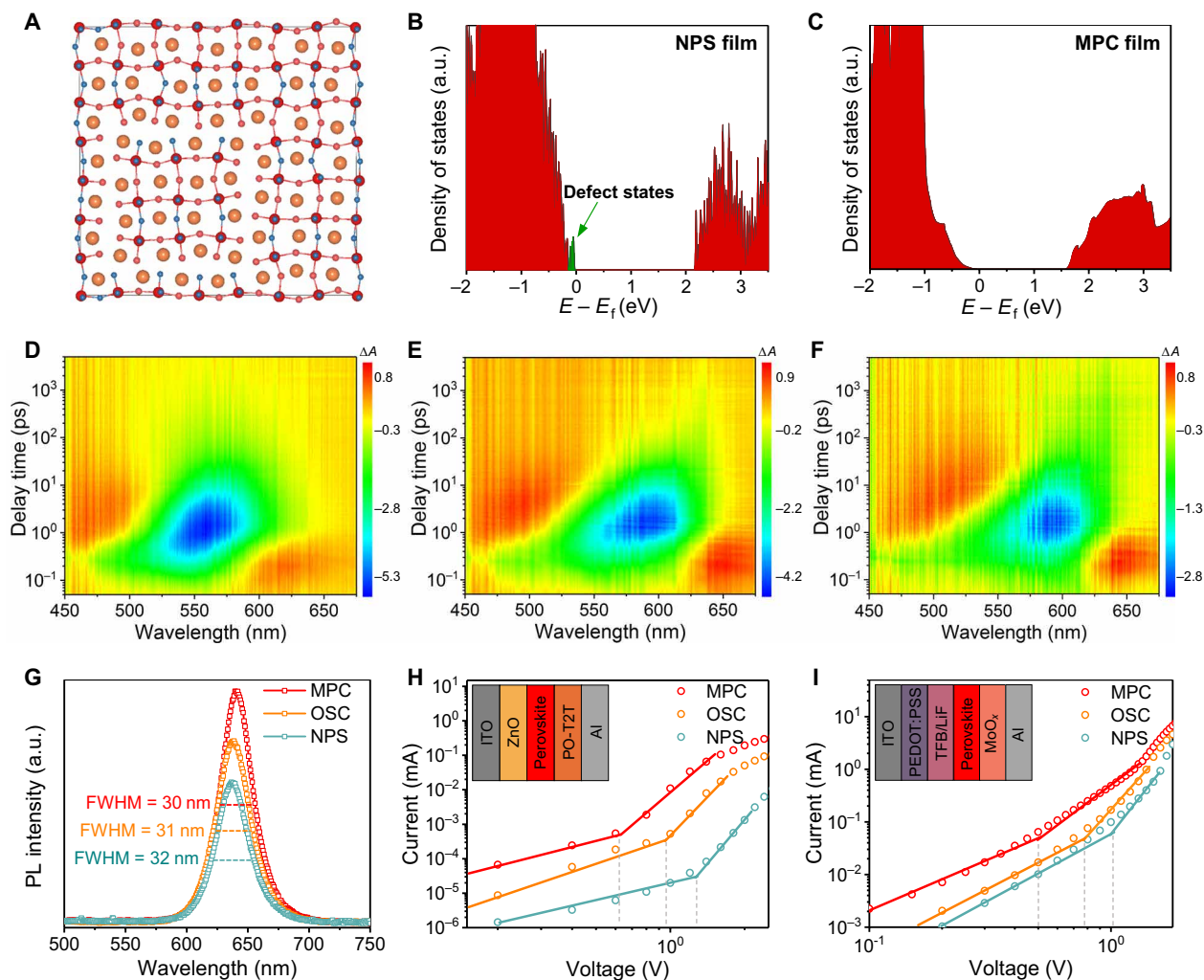
Fig. 4. Effect of RP defects on the perovskite thin film bandgap and optoelectronic properties. (**A**) Lattice model of NPS film with the 2D RP defect–restricted region. Colors of the balls represent the following: orange, cesium; red, lead; blue, bromine; and magenta, iodine. (**B**) Density-of-states (DOS) plots of NPS film with 2D RP defect–restricted region. (**C**) DOS plots of MPC film with planar defect–free lattice. Depicted in red and green in the DOS are the band and the isolated defect states induced by the RP lattice mismatch, respectively. a.u., arbitrary units. (**D** to **F**) Contour maps of the fs-TA spectra recorded on NPS (D), OSC (E), and MPC (F) thin films. (**G**) Steady-state PL emission spectra. FWHM, full width at half maximum. (**H** and **I**) Current-voltage curves of (H) electron-only and (I) hole-only devices under dark conditions. Insets are their corresponding device structures. ITO, indium tin oxide; PEDOT:PSS, poly(3,4-ethylenedioxythiophene) polystyrene sulfonate; LIF, lithium fluoride; TFB, poly(9,9-dioctylfluorene-co-N-(4-butylphenyl) diphenylamine); Al, aluminum.

RP defect-free CsPbI$_{3-x}$Br$_x$ thin films for efficient and bright pure red LEDs

Encouraged by the excellent optoelectronic properties of MPC thin films, we fabricated LEDs with the planar structure of indium tin oxide (ITO; as anode, 100 nm)/poly(3,4-ethylenedioxythiophene) polystyrene sulfonate (PEDOT:PSS), poly(N,N′-bis-4-butylphenyl-N,N′-bisphenyl) benzidine (poly-TPD), poly(9,9-dioctylfluorene-co-N-(4-butylphenyl) diphenylamine) (TFB), and lithium fluoride (LiF; as the hole transport layer, about 50 nm)/perovskite (the emission layer, about 30 nm)/2,4,6-tris[3-(diphenylphosphinyl)phenyl]-1,3,5-triazine (PO-T2T; as the electron transport layer, about 70 nm)/LiF (as the electron injection layer, about 1 nm)/aluminum (Al; as cathode, about 100 nm) (Fig. 5A and figs. S26 and S27). The LED based on the MPC thin film exhibits a low turn-on voltage of 2.2 V, a high maximum luminance of 7000 cd m^{-2}, and a high EQE of 13.9% (Fig. 5, B and C). Note that the EQE of the MPC device was

much higher than that of the NPS (5.8%) and OSC (6.3%) devices, indicating that the elimination of intragrain RP planar defects can substantially improve the electroluminescence (EL) performance. Furthermore, we used octylammonium sulfate solution to treat the MPC film (MPC with SO$_4^{2-}$) for further reducing the surface defects of the MPC thin film (fig. S28). The LED based on the MPC thin film coated with SO$_4^{2-}$ achieved a maximum EQE of 17.8% and a maximum brightness of 9000 cd m^{-2} with color coordinates of (0.706, 0.294), which represents the best performance for pure red solution-processed perovskite LED devices to date (figs. S29 and S30 and table S3).

Besides the efficiency and brightness, the EL spectral stability of the mixed halide perovskite LED is usually very low because the defects including our identified PR planar defects would be the high-speed ion migration sites in the thin films (fig. S31, A and B). We tested the EL spectral stability of the LED devices based on different CsPbI$_{3-x}$Br$_x$
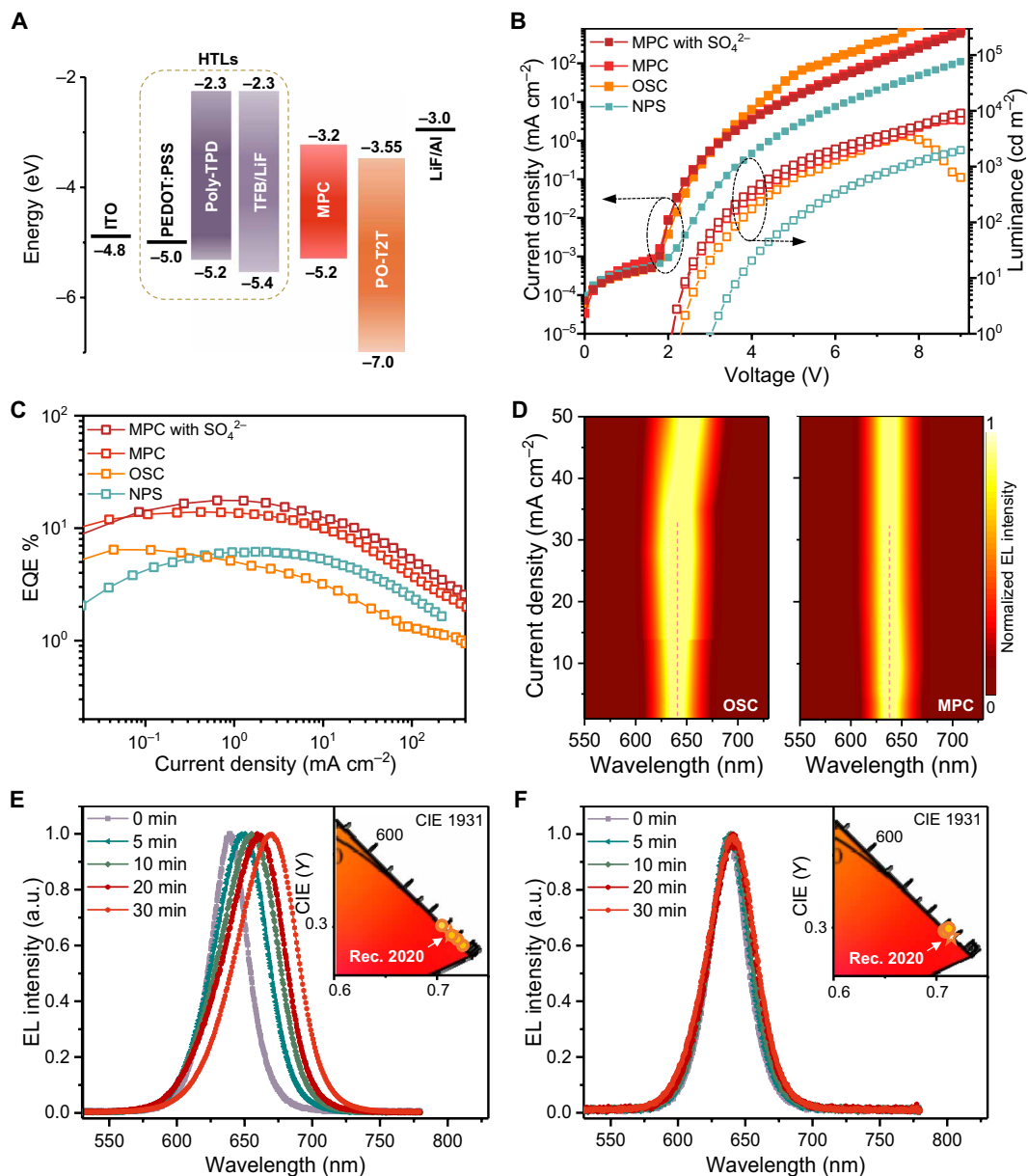
Fig. 5. Performance evaluation of mixed halide CsPbI$_{3-x}$Br$_x$ LED devices. (**A**) Flat band energy level diagram of the device. HTLs, hole transporting layers. (**B** and **C**) Current density–luminance–voltage characteristics (B) and the corresponding EQE–current density relationship (C) of the fabricated LED devices. (**D**) EL spectral stability as a function of current density for OSC and MPC CsPbI$_{3-x}$Br$_x$ LEDs. (**E** and **F**) Normalized EL spectra of the pure red LED based on OSC (E) and MPC for SO$_4^{2-}$ (F) at 1 mA cm^{-2} with different operational times. Insets show the corresponding color-coordinated shift. CIE, commission internationale d'Eclairage.

thin films at a fixed current density over time and over a range of current densities. As for MPC thin film–based LED, the EL spectrum is stable at 638 nm at a current density of 50 mA cm^{-2} and only exhibits a 5-nm red shift even at a high-current density of 200 mA cm^{-2}. In contrast, more than a 15-nm red shift was observed for the LED based on the OSC thin film only at a current density of 50 mA cm^{-2} (Fig. 5D and fig. S31, C and D). Furthermore, we tested the EL spectrum stability of the LED devices at 1 mA cm^{-2}. The EL spectrum of the LED based on the MPC thin film with SO$_4^{2-}$ can be maintained for 30 min without obvious change in color coordinates, whereas the large EL broadening and the color-coordinated shifting were observed in the OSC film–based LED (Fig. 5, E and F). In addition, we tested the EL

compared to the quick spectral red shift of the LED based on OSC thin film operated at 10 mA cm^{-2}, the EL spectrum of the MPC thin film–based LED remains relatively stable at 640 nm within 10 min, and the time for the EL intensity decay to 50% of its initial value (T_{50}) of the MPC thin film–based LED is 40 min, which is sixfold of the LED based on OSC thin film (fig. S32). Moreover, we used the square wave with a frequency of 50 Hz, a recovering bias of −1 V, and a duty ratio of 20% to drive the devices (figs. S33 and S34), considering that the reverse bias could promote the rearrangement of halide ions in the mixed halide thin films to further improve the EL spectrum stability. For the LEDs driven by the square wave of 1 mA cm^{-2}, the EL spectrum of the LED based on the MPC thin film with

SO_4^{2-} can be maintained at 640 nm over 120 min without obvious change in color coordinates, whereas the large EL broadening of the color-coordinated shift was still observed in the OSC film–based LED due to the migration of halide ions (fig. S35). In contrast, we tried octylammonium sulfate solution to treat the NPS and OSC films (NPS with SO_4^{2-} and OSC with SO_4^{2-}) for further reducing the defects of the NPS and OSC thin films and improving the EL spectrum stability (fig. S36). However, the intragrain RP defects cannot be efficiently eliminated in the NPS and OSC films with SO_4^{2-}, and thus the EL spectral broadening and red shifting were still observed. As for the MPC-based LED devices with different halogen ratios, the EL spectral red shift was less than 3 nm under the square wave voltage operation for 60 min, which indicates that our MPC strategy is effective for other halogen ratios of the perovskite thin films (fig. S37). Therefore, eliminating the RP defects via MPC is effective to suppress the migration of halogen ions in the mixed halide $CsPbI_{3-x}Br_x$ perovskite for stabilizing LEDs.

DISCUSSION

In summary, we identified the widespread existence of intragrain RP planar defects in the mixed halide $CsPbI_{3-x}Br_x$ thin films prepared via conventional OSC, which are the main causes of poor performance of the fabricated pure red perovskite light-emitting diodes (PeLEDs). To eliminate these planar defects, we developed a stepwise MPC strategy to obtain planar defect–free $CsPbI_{3-x}Br_x$ thin films with improved radiative recombination, narrowed emission band, and enhanced spectral stability. Our developed MPC strategy consisted of a reorganization step of a metastable precursor and a crystallization step of the metastable phase, resulting in minimized lattice strain in the $CsPbI_{3-x}Br_x$ perovskite with homogeneous halogen distribution to avoid the formation of RP planar defects. The elimination of the planar defects can efficiently improve the optoelectronic properties of the obtained $CsPbI_{3-x}Br_x$ thin films, enabling us to fabricate spectrally stable pure red PeLEDs with a high EQE of 17.8%, a luminance of 9000 cd m^{-2}, and a spectral stability of up to 120 min. Our MPC strategy paves the way to fabricate low-defect density mixed halide perovskite thin films, which can be readily applied in the fabrication of high-performance pure color PeLEDs.

MATERIALS AND METHODS
Materials
The following materials are used in this study: DMF (anhydrous; 99.8%; Sigma-Aldrich); lead bromide ($PbBr_2$, 99.999%), cesium bromide (CsBr; 99.999%), and lead iodide (PbI_2; 99.999%) were bought from Xi'an Polymer Light Technology Corp.; L-arginine ($C_6H_{14}N_4O_2$; 98%; Aladdin); PVDF-HFP [average weight-average molecular weight (M_w) ≈ 400,000; Sigma-Aldrich]; PEDOT:PSS solution (Clevios, PVP Al4083); TFB (Luminescence Technology Corp.); chlorobenzene (C_6H_5Cl; anhydrous; Aladdin); LiF (99.99%; Lumtech Corp.); and PO-T2T (99%; Nichem).

Preparation of mixed halide $CsPbI_{3-x}Br_x$ perovskite thin films
$CsPbI_{3-x}Br_x$ perovskite thin film without any additive
The $CsPbI_{3-x}Br_x$ precursor solution was prepared by dissolving 0.12 mmol of CsI, 0.025 mmol of CsBr, 0.037 mmol of PbI_2, and 0.06 mmol of $PbBr_2$ in 1 ml of DMF and stirring at 60°C for 1 hour

in an N_2-filled glove box. The precursor was diluted to 0.065 M for the following spin coating. The perovskite was spin-coated from the precursor solution at 8000 revolutions per minute (rpm) for 50 s followed by annealing at 90°C for 10 min and then 120°C for 5 min.

NPS $CsPbI_{3-x}Br_x$ perovskite thin film
The NPS thin film precursor solution was prepared by dissolving 0.12 mmol of CsI, 0.025 mmol of CsBr, 0.037 mmol of PbI_2, 0.06 mmol of $PbBr_2$, and 0.017 mmol of L-Arg in 1 ml of DMF and by stirring at 60°C for 1 hour in an N_2-filled glove box. The precursor was diluted to 0.065 M for the following spin coating. The perovskite was spin-coated from the precursor solution at 8000 rpm for 50 s followed by annealing at 90°C for 10 min and then at 120°C for 5 min.

OSC $CsPbI_{3-x}Br_x$ perovskite thin film
The OSC thin film precursor solution was prepared by adding 50 μl of PVDF-HFP solution (50 mg ml^{-1}) into 800 μl of NPS thin-film precursor solution (0.1 M based on lead) and then diluted to 0.065 M for the following spin coating. The perovskite was spin-coated from the precursor solution at 8000 rpm for 50 s followed by annealing at 110°C for 15 min.

MPC $CsPbI_{3-x}Br_x$ perovskite thin film
The MPC thin-film precursor solution was prepared by adding 50 μl of PVDF-HFP solution (50 mg ml^{-1}) into 800 μl of NPS thin-film precursor solution (0.1 M based on lead) and then diluted to 0.065 M for the following spin coating. The thin film was spin-coated from the precursor solution at 8000 rpm for 50 s followed by annealing at 90°C for 10 min and then at 120°C for 5 min. For the MPC with SO_4^{2-} film, the MPC film was annealed at 90°C for 10 min and then treated with 1 mM octylammonium sulfate solution [prepared by adding 5.33 μl of concentrated sulfuric acid and 33.05 μl of octylammonium into 100 ml of mixed solvents (n-octane/isopropanol = 8:1)] for 35 s after cooling and then heated to 120°C for 5 min.

Preparation of TEM samples
The ultrathin carbon film–coated copper grid was attached to the glass substrate by polyimide tape, and the substrate was cleaned with ethanol solution and ozone treatment for 8 min before preparing the perovskite thin film for TEM characterization. The perovskite thin films with different components were spin-coated from the precursor solution at 8000 rpm for 50 s followed by different annealing process. Last, the copper grid was carefully clipped from the glass substrate and then loaded into TEM chamber for the characterization.

Computational methods
We carried out all periodic density functional theory (DFT) calculations using Vienna Ab Initio Simulation Package (35, 36). The popular Perdew-Burke-Ernzerhof (37) functional and projector augmented wave (38, 39) potentials in conjunction with a plane-wave basis set of 400-eV cutoff were used throughout the computation. By using the cubic $CsPbBr_3$ unit cell as the prototype, we made an 8 × 8 × 1 supercell, removed a proper number of Pb and Br atoms (making trench-like defects), and realigned atoms on the two sides of trenches to 2D RP defects, as found in the atomic resolution HAADF-STEM images (Fig. 2). To represent the experimentally synthesized $CsPbI_{3-x}Br_x$ samples, we replaced Br atoms with I atoms in a 1:1 ratio. In addition, we adopted a 2 × 1 × 1 supercell to represent a defect-free $CsPbI_{3-x}Br_x$. For the sampling of the Brillouin zone, we applied the Monkhorst-Pack scheme (40) to generate 3 × 6 × 6, 1 × 7 × 7, and 1 × 1 × 7 k-point grids for 2 × 1 × 1, 8 × 1 × 1, and 8 × 8 × 1 supercells, respectively. The convergence criteria for geometry

optimization were set to 0.02 eV Å^{-1} for force per atom and 10^{-5} eV for total energy.

LED device fabrication

ITO-coated glass substrates were ultrasonically cleaned at least three times by soap solution, deionized water mixed with ethanol, acetone mixed with ethanol, and ethanol in sequence and then treated by ultraviolet ozone for 15 min. The PEDOT:PSS solution was spun at 4000 rpm for 50 s and then annealed at 140°C for 20 min under ambient conditions. Poly-TPD in C_6H_5Cl (6 mg ml^{-1}) and TFB in C_6H_5Cl (4 mg ml^{-1}) were sequentially spin-coated on the PEDOT:PSS layer at 4000 rpm for 50 s and annealed at 120°C on a hot plate for 10 min under a N_2 atmosphere. Then, 1 nm of LiF was evaporated at a pressure of 10^{-5} mbar. Subsequently, the perovskite films with different components were spin-coated from the precursor solution at 8000 rpm for 50 s followed by the corresponding annealing process. For the MPC with SO_4^{2-} film, the perovskite film was annealed at 90°C for 10 min and was treated with 1 mM octylammonium sulfate solution for 35 s after cooling and then heated to 120°C for 5 min. Afterward, PO-T2T (40 nm) and LiF/Al electrodes (1 nm/100 nm) were deposited using a thermal evaporation system through a shadow mask (active pixel area, 4 mm^2) under a high vacuum of $\sim 2 \times 10^{-4}$ Pa. All operations were carried out under the conditions of ambient temperature below 25°C.

Device performance measurement

For the as-fabricated LED device performance test, a Keithley 2400 Source Meter was used to record the current versus voltage characteristics. The luminescence of the device was revealed by photon flux using a silicon photodiode, which was calibrated by a PR-670 spectral scan luminance meter. The EL spectrum of the device was collected using an Ocean Optics JAZ spectrometer. Other important parameters used to characterize LEDs were all calculated from the Current density-luminance-Voltage and EL measurements under the assumption that the emission of the LEDs exhibits a Lambertian pattern. The measurements for devices were performed at room temperature under a N_2 atmosphere. The EL spectral stability of the LEDs was tested at a brightness of 100 cd cm^{-2} using square wave alternating voltage. By testing the spectral stability of the devices at different frequencies, different duty ratios, and different reverse voltages, last, we used the square wave with 50 Hz, 20% duty ratio, and a −1V reverse voltage.

Characterizations

TEM measurements

The TEM images were acquired on a Hitachi HT-7700 transmission electron microscope with an accelerating voltage of 120 kV. Atomic resolution HAADF-STEM images were obtained on probe aberration-corrected JEM-ARM200F (S) TEM operated at 200 kV. The total electron dose is the key parameter that determines the degree of structural damage and must be taken into account when preparing EM experiments for halide perovskites. The all-inorganic perovskite can maintain stable lattice under the critical electron dose at the scale of $\approx 10^2$ to 10^5 e Å^{-2}, so it is possible to perform HRTEM and STEM studies for all-inorganic MHPs (41). To minimize possible electron beam–induced damage, we used low-dose STEM characterization with an electron dose rate of 5617.4 e Å^{-2} for the MPC sample, 1943.7 e Å^{-2} for the OSC sample, and 2097.1 e Å^{-2} for the NPS sample. The fast Fourier transform (FFT) patterns were obtained by using a DigitalMicrograph software on the corresponding data.

For the analysis of lattice mismatch caused by defects, we adopted the following formula of lattice constant strain

$$\varepsilon_{mis} = \frac{d - d_0}{d_0} \times 100\%$$

where ε_{mis} is the lattice mismatch, d_0 is the normal lattice constant, and d is the abnormal lattice constant.

The strain strainmaps were obtained by using a StatSTEM software to analyze the atomic phase of the MPC, OSC, and NPS samples (42). We set the unit cell parameter of the normal lattice to be 0.605 nm and then obtained the strain mapping diagram according to the degree of deviation between adjacent atoms from the normal lattice.

HRTEM images were acquired on a FEI Talos F200X transmission electron microscope at an accelerating voltage of 200 kV. The electron beam energy was adjusted to the minimum value of the instrument and shot TEM dates as fast as possible to minimize the damage of the electron beam to the perovskite film. Low-magnification HAADF-STEM and EDS elemental mapping were acquired on a FEI Talos F200X transmission electron microscope at an accelerating voltage of 200 kV equipped with four silicon drift detectors. To minimize the degradation of the perovskite thin films caused by the environment, all the perovskite samples were sealed in a N_2 filled container immediately after annealing, and these samples were exposed to ambient conditions for less than 5 min before the characterization. Unless otherwise specified, all perovskite samples used for characterization were prepared in the same way as the preparation process of the perovskite thin film in the device.

Morphology and crystallization measurements

The cross-section morphology of device was collected by scanning electron microscope (Carl Zeiss Supra 40) at an acceleration voltage of 5 kV. The AFM images were collected by using a Veeco DI Nanoscope V system with a tapping mode. The powder XRD patterns were recorded using a Philips X'Pert Pro Super XRD equipped with graphite monochromatized Cu Kα radiation.

Solution ^{1}H NMR

^{1}H nuclear magnetic resonance (NMR) measurements were recorded on a Bruker Avance III high-definition spectrometer operating at a ^{1}H frequency of 400 MHz and equipped with a Double Resonance Broad Band ^{19}F (BBFO-Z) probe. A total of 0.017 mmol of L-Arg was dispersed in 1 ml of $(CD_3)_2SO$ and stirred at 60°C for 1 hour in an argon-filled glove box. $CsPbI_{3-x}Br_x$ with L-Arg precursor solution was prepared as mentioned in the NPS solution [0.12 mmol of CsI, 0.025 mmol of CsBr, 0.037 mmol of PbI_2, and 0.06 mmol of $PbBr_2$ in 1 ml of $(CD_3)_2SO$] and stirred at 60°C for 1 hour in an N_2-filled glove box. The precursor solution was diluted to 0.065 M.

Optical characterizations

The PL spectra were collected on a Hamamatsu absolute PL yield spectrometer C11347 using a 365-nm excitation at room temperature. The PL kinetics (excited at 400 nm and monitored at 485 nm) was recorded on an FLS920 fluorescence spectrometer (Edinburgh) under ambient conditions. The data acquisition was based on TC-SPC. The 400-nm excitation was provided by an SC400-2 supercontinuum laser source (Fianium) with a 6-ps pulse width and a 5-MHz repetition rate. The PL lifetimes were obtained by a standard tail fit using the F900 software. The fs-TA measurements were performed on a pump-probe system (Helios, Ultrafast Systems LLC) in combination with an amplified laser system (Coherent) under ambient conditions. The pump pulses (center wavelength of 400 nm, ~20 nJ

per pulse at the sample cell) were delivered by an optical parametric amplifier (TOPAS-800-fs), excited by a Ti:sapphire-regenerative amplifier (800 nm, 35 fs, 3 mJ per pulse; Legend Elite-1 K-HE), seeded with a mode-locked Ti:sapphire laser system (Micra-5), and pumped with a Neodymium: Yttrium Lithium Fluoride (Nd:YLF) laser (Evolution 30). The white-light continuum (WLC) probe pulses (430 to 620 nm) were generated by focusing the 800-nm beam (split from the regenerative amplifier, ~400 nJ per pulse) onto a sapphire plate. A reference beam split from the WLC was used to correct the pulse-to-pulse fluctuation of the WLC for achieving a best signal-to-noise ratio. The time delay between the pump and probe pulses was varied by a motorized optical delay line (maximum of ~8 ns). The instrument response function was determined to be ~100 fs by a routine cross-correlation procedure. A chopper operating at 500 Hz was used to modulate the pump pulses, such that the fs-TA spectra with and without the pump pulses can be recorded alternately. The temporal and spectral profiles of the pump-induced differential transmission of the WLC probing light (or absorbance change) were registered by an optical fiber–coupled multichannel spectrometer with a complementary metal-oxide semiconductor sensor and further processed by the SURFACE XPLORER software.

Ultraviolet photoelectron spectroscopy characterization

Ultraviolet photoelectron spectroscopy (UPS) spectra of $CsPbI_{3-x}Br_x$ on glass were measured on a Thermo ESCALAB 250 spectrometer using He I radiation (21.2 eV).

Residual DMF content measurement

Gas chromatography (GC) was tested using Thermo Q Exactive GC. The NPS and MPC precursor solutions were sequentially spin-coated on a 1.7–by–1.7 cm square glass substrate at 8000 rpm for 50 s, and then the perovskite films were annealed on a 90°C heating plate for 2, 5, and 10 min, respectively. For each GC sample, two perovskite films based on 1.7–by–1.7 cm glass substrates were immersed in 1 ml of acetone solvent for 1 day to replace the DMF in the sample. Then, we blew the solution into the test instrument (Thermo Q Exactive GC) and lastly obtained the residual DMF content in the sample by comparison with the peak area of the 10^{-5} g of DMF/acetone solution.

Trap density characterization

For electron-only devices, the ZnO solution was spun at 8000 rpm for 50 s and then annealed at 150°C for 15 min to achieve a layer thickness of ~30 nm under ambient conditions. The perovskite films with different components were spin-coated from the precursor solution at 8000 rpm for 50 s followed by corresponding annealing process as mentioned before. Afterward, PO-T2T (40 nm) and LiF/Al electrodes (1 nm/100 nm) were deposited using a thermal evaporation system through a shadow mask (active pixel area, 4 mm^2) under a high vacuum of ~2 × 10^{-4} Pa. For hole-only devices, The PEDOT:PSS solution was spun at 4000 rpm for 50 s and then annealed at 140°C for 20 min under ambient conditions. Poly-TPD in C_6H_5Cl (6 mg ml^{-1}) and TFB in C_6H_5Cl (4 mg ml^{-1}) were sequentially spin-coated on the PEDOT:PSS layer at 4000 rpm for 50 s and annealed at 120°C on a hot plate for 10 min under a N_2 atmosphere. Then, 1 nm of LiF was thermally evaporated at a pressure of ~2 × 10^{-4} Pa. Subsequently, the perovskite films with different components were spin-coated from the precursor solution at 8000 rpm for 50 s followed by corresponding annealing process. Afterward, MoO_3 (10 nm) and LiF/Al electrodes (1 nm/100 nm) were deposited using a thermal evaporation system through a shadow mask (active pixel area, 4 mm^2) under a vacuum of ~2 × 10^{-4} Pa.

For the SCLC measurement, the electron-only or hole-only device will first exhibit an ohmic behavior, in which current varies linearly at low voltage. When the voltage is increased to an inflection point, the devices exhibit the filling process of trap, in which current exhibits a nonlinear rise, and the voltage at the intersection point between the linear and nonlinear region is defined as the trap-filled limit voltage (V_{TFL}). The trap state densities (N_{trap}) is determined by using the equation

$$N_{trap} = \frac{2\varepsilon\varepsilon_0}{eL^2} V_{TFL}$$

where ε_0 is the vacuum permittivity, ε is the relative permittivity of perovskite, V_{TFL} is the trap-filled limit voltage, e is the elementary charge, and L is the thickness of the perovskite film.

REFERENCES AND NOTES

1. X. K. Liu, W. Xu, S. Bai, Y. Jin, J. Wang, R. H. Friend, F. Gao, Metal halide perovskites for light-emitting diodes. *Nat. Mater.* **20**, 10–21 (2021).

2. Y. Liu, J. Cui, K. Du, H. Tian, Z. He, Q. Zhou, Z. Yang, Y. Deng, D. Chen, X. Zuo, Y. Ren, L. Wang, H. Zhu, B. Zhao, D. Di, J. Wang, R. H. Friend, Y. Jin, Efficient blue light-emitting diodes based on quantum-confined bromide perovskite nanostructures. *Nat. Photon.* **13**, 760–764 (2019).

3. M. Yuan, L. N. Quan, R. Comin, G. Walters, R. Sabatini, O. Voznyy, S. Hoogland, Y. Zhao, E. M. Beauregard, P. Kanjanaboos, Z. Lu, D. H. Kim, E. H. Sargent, Perovskite energy funnels for efficient light-emitting diodes. *Nat. Nanotechnol.* **11**, 872–877 (2016).

4. N. Wang, L. Cheng, R. Ge, S. Zhang, Y. Miao, W. Zou, C. Yi, Y. Sun, Y. Cao, R. Yang, Y. Wei, Q. Guo, Y. Ke, M. Yu, Y. Jin, Y. Liu, Q. Ding, D. Di, L. Yang, G. Xing, H. Tian, C. Jin, F. Gao, R. H. Friend, J. Wang, W. Huang, Perovskite light-emitting diodes based on solution-processed self-organized multiple quantum wells. *Nat. Photon.* **10**, 699–704 (2016).

5. H. C. Cho, S. H. Jeong, M. H. Park, Y. H. Kim, C. Wolf, C. L. Lee, J. H. Heo, A. Sadhanala, N. Myoung, S. Yoo, S. H. Im, R. H. Friend, T. W. Lee, Overcoming the electroluminescence efficiency limitations of perovskite light-emitting diodes. *Science* **350**, 1222–1225 (2015).

6. Z. K. Tan, R. S. Moghaddam, M. L. Lai, P. Docampo, R. Higler, F. Deschler, M. Price, A. Sadhanala, L. M. Pazos, D. Credgington, F. Hanusch, T. Bein, H. J. Snaith, R. H. Friend, Bright light-emitting diodes based on organometal halide perovskite. *Nat. Nanotechnol.* **9**, 687–692 (2014).

7. K. Lin, J. Xing, L. N. Quan, F. P. G. de Arquer, X. Gong, J. Lu, L. Xie, W. Zhao, D. Zhang, C. Yan, W. Li, X. Liu, Y. Lu, J. Kirman, E. H. Sargent, Q. Xiong, Z. Wei, Perovskite light-emitting diodes with external quantum efficiency exceeding 20 per cent. *Nature* **562**, 245–248 (2018).

8. W. Li, M. U. Rothmann, Y. Zhu, W. Chen, C. Yang, Y. Yuan, Y. Y. Choo, X. Wen, Y.-B. Cheng, U. Bach, J. Etheridge, The critical role of composition-dependent intragrain planar defects in the performance of $MA_{1-x}FA_xPbI_3$ perovskite solar cells. *Nat. Energy* **6**, 624–632 (2021).

9. Z. Ni, C. Bao, Y. Liu, W.-Q. Wu, S. Chen, X. Dai, B. Chen, B. Hartweg, Z. Yu, Z. Holman, J. Huang, Resolving spatial and energetic distributions of trap states in metal halide perovskite solar cells. *Science* **367**, 1352–1358 (2020).

10. M. I. Saidaminov, J. Kim, A. Jain, R. Quintero-Bermudez, H. Tan, G. Long, F. Tan, A. Johnston, Y. Zhao, O. Voznyy, E. H. Sargent, Suppression of atomic vacancies via incorporation of isovalent small ions to increase the stability of halide perovskite solar cells in ambient air. *Nat. Energy* **3**, 648–654 (2018).

11. J. M. Ball, A. Petrozza, Defects in perovskite-halides and their effects in solar cells. *Nat. Energy* **1**, 16149 (2016).

12. T. A. S. Doherty, A. J. Winchester, S. Macpherson, D. N. Johnstone, V. Pareek, E. M. Tennyson, S. Kosar, F. U. Kosasih, M. Anaya, M. Abdi-Jalebi, Z. Andaji-Garmaroudi, E. L. Wong, J. Madeo, Y. H. Chiang, J. S. Park, Y. K. Jung, C. E. Petoukhoff, G. Divitini, M. K. L. Man, C. Ducati, A. Walsh, P. A. Midgley, K. M. Dani, S. D. Stranks, Performance-limiting nanoscale trap clusters at grain junctions in halide perovskites. *Nature* **580**, 360–366 (2020).

13. C. Sun, Y. Jiang, M. Cui, L. Qiao, J. Wei, Y. Huang, L. Zhang, T. He, S. Li, H. Y. Hsu, C. Qin, R. Long, M. Yuan, High-performance large-area quasi-2D perovskite light-emitting diodes. *Nat. Commun.* **12**, 2207 (2021).

14. L. Zhu, H. Cao, C. Xue, H. Zhang, M. Qin, J. Wang, K. Wen, Z. Fu, T. Jiang, L. Xu, Y. Zhang, Y. Cao, C. Tu, J. Zhang, D. Liu, G. Zhang, D. Kong, N. Fan, G. Li, C. Yi, Q. Peng, J. Chang,

X. Lu, N. Wang, W. Huang, J. Wang, Unveiling the additive-assisted oriented growth of perovskite crystallite for high performance light-emitting diodes. *Nat. Commun.* **12**, 5081 (2021).

15. L. Kong, X. Zhang, Y. Li, H. Wang, Y. Jiang, S. Wang, M. You, C. Zhang, T. Zhang, S. V. Kershaw, W. Zheng, Y. Yang, Q. Lin, M. Yuan, A. L. Rogach, X. Yang, Smoothing the energy transfer pathway in quasi-2D perovskite films using methanesulfonate leads to highly efficient light-emitting devices. *Nat. Commun.* **12**, 1246 (2021).

16. Y. Jiang, M. Cui, S. Li, C. Sun, Y. Huang, J. Wei, L. Zhang, M. Lv, C. Qin, Y. Liu, M. Yuan, Reducing the impact of Auger recombination in quasi-2D perovskite light-emitting diodes. *Nat. Commun.* **12**, 336 (2021).

17. D. Ma, K. Lin, Y.-K. Wang, B. Chen, Y. Dong, H. Choubisa, A. H. Proppe, D. Wu, P. Li, J. Z. Fan, Y. Liu, A. Johnston, Y. Kang, F. Yuan, Z.-H. Lu, Z. Wei, E. H. Sargent, Distribution control enables efficient reduced-dimensional perovskite LEDs. *Nature* **599**, 594–598 (2021).

18. Z. Liu, W. Qiu, X. Peng, G. Sun, X. Liu, D. Liu, Z. Li, F. He, C. Shen, Q. Gu, F. Ma, H.-L. Yip, L. Hou, Z. Qi, S.-J. Su, Perovskite light-emitting diodes with EQE exceeding 28% through a synergetic dual-additive strategy for defect passivation and nanostructure regulation. *Adv. Mater.* **33**, 2103268 (2021).

19. Y. Cao, N. Wang, H. Tian, J. Guo, Y. Wei, H. Chen, Y. Miao, W. Zou, K. Pan, Y. He, H. Cao, Y. Ke, M. Xu, Y. Wang, M. Yang, K. Du, Z. Fu, D. Kong, D. Dai, Y. Jin, G. Li, H. Li, Q. Peng, J. Wang, W. Huang, Perovskite light-emitting diodes based on spontaneously formed submicrometre-scale structures. *Nature* **562**, 249–253 (2018).

20. W. Xu, Q. Hu, S. Bai, C. Bao, Y. Miao, Z. Yuan, T. Borzda, A. J. Barker, E. Tyukalova, Z. Hu, M. Kawecki, H. Wang, Z. Yan, X. Liu, X. Shi, K. Uvdal, M. Fahlman, W. Zhang, M. Duchamp, J.-M. Liu, A. Petrozza, J. Wang, L.-M. Liu, W. Huang, F. Gao, Rational molecular passivation for high-performance perovskite light-emitting diodes. *Nat. Photon.* **13**, 418–424 (2019).

21. Y. Zou, P. Teng, W. Xu, G. Zheng, W. Lin, J. Yin, L. Kobera, S. Abbrent, X. Li, J. A. Steele, E. Solano, M. B. J. Roeffaers, J. Li, L. Cai, C. Kuang, I. G. Scheblykin, J. Brus, K. Zheng, Y. Yang, O. F. Mohammed, O. M. Bakr, T. Pullerits, S. Bai, B. Sun, F. Gao, Manipulating crystallization dynamics through chelating molecules for bright perovskite emitters. *Nat. Commun.* **12**, 4831 (2021).

22. K. H. Wang, L. Wang, Y. Y. Liu, Y. H. Song, Y. C. Yin, J. S. Yao, J. N. Yang, J. J. Wang, L. Z. Feng, Q. Zhang, Q. Zhang, H. B. Yao, High quality CsPbI$_{3-x}$Br$_x$ thin films enabled by synergetic regulation of fluorine polymers and amino acid molecules for efficient pure red light emitting diodes. *Adv. Opt. Mater.* **9**, 2001684 (2021).

23. Y. Tian, C. Zhou, M. Worku, X. Wang, Y. Ling, H. Gao, Y. Zhou, Y. Miao, J. Guan, B. Ma, Highly efficient spectrally stable red perovskite light-emitting diodes. *Adv. Mater.* **30**, e1707093 (2018).

24. J. Qing, S. Ramesh, Q. Xu, X. K. Liu, H. Wang, Z. Yuan, Z. Chen, L. Hou, T. C. Sum, F. Gao, Spacer cation alloying in Ruddlesden-Popper perovskites for efficient red light-emitting diodes with precisely tunable wavelengths. *Adv. Mater.* **33**, 2104381 (2021).

25. K. Qasim, B. Wang, Y. Zhang, P. Li, Y. Wang, S. Li, S.-T. Lee, L.-S. Liao, W. Lei, Q. Bao, Solution-processed extremely efficient multicolor perovskite light-Emitting diodes utilizing doped electron transport layer. *Adv. Funct. Mater.* **27**, 1606874 (2017).

26. Y. Ke, N. Wang, D. Kong, Y. Cao, Y. He, L. Zhu, Y. Wang, C. Xue, Q. Peng, F. Gao, W. Huang, J. Wang, Defect passivation for red perovskite light-emitting diodes with improved brightness and stability. *J. Phys. Chem. Lett.* **10**, 380–385 (2019).

27. W.-J. Yin, T. Shi, Y. Yan, Unusual defect physics in CH$_3$NH$_3$PbI$_3$ perovskite solar cell absorber. *Appl. Phys. Lett.* **104**, 063903 (2014).

28. A. Walsh, D. O. Scanlon, S. Chen, X. G. Gong, S. H. Wei, Self-regulation mechanism for charged point defects in hybrid halide perovskites. *Angew. Chem. Int. Ed.* **54**, 1791–1794 (2015).

29. L. B. Mao, H. L. Gao, H. B. Yao, L. Liu, H. Colfen, G. Liu, S. M. Chen, S. K. Li, Y. X. Yan, Y. Y. Liu, S. H. Yu, Synthetic nacre by predesigned matrix-directed mineralization. *Science* **354**, 107–110 (2016).

30. T. Schilling, H. J. Schöpe, G. Oettel, I. Snook, Precursor-mediated crystallization process in suspensions of hard spheres. *Phys. Rev. Lett.* **105**, 025701 (2010).

31. Y. Peng, F. Wang, Z. Wang, A. M. Alsayed, Z. Zhang, A. G. Yodh, Y. Han, Two-step nucleation mechanism in solid-solid phase transitions. *Nat. Mater.* **14**, 101–108 (2015).

32. Y. Dong, Y. K. Wang, F. Yuan, A. Johnston, Y. Liu, D. Ma, M. J. Choi, B. Chen, M. Chekini, S. W. Baek, L. K. Sagar, J. Fan, Y. Hou, M. Wu, S. Lee, B. Sun, S. Hoogland, R. Quintero-Bermudez, H. Ebe, P. Todorovic, F. Dinic, P. Li, H. T. Kung, M. I. Saidaminov, E. Kumacheva, E. Spiecker, L. S. Liao, O. Voznyy, Z. H. Lu, E. H. Sargent, Bipolar-shell resurfacing for blue LEDs based on strongly confined perovskite quantum dots. *Nat. Nanotechnol.* **15**, 668–674 (2020).

33. A. Swarnkar, A. R. Marshall, E. M. Sanehira, B. D. Chernomordik, D. T. Moore, J. A. Christians, T. Chakrabarti, J. M. Luther, Quantum dot–induced phase stabilization of α-CsPbI$_3$ perovskitefor high-efficiency photovoltaics. *Science* **354**, 92–95 (2016).

34. M. T. Trinh, X. Wu, D. Niesner, X.-Y. Zhu, Many-body interactions in photo-excited lead iodide perovskite. *J. Mater. Chem. A* **3**, 9285–9290 (2015).

35. G. Kresse, Efficient iterative schemes for ab initio total-energy calculations using a plane-wave basis set. *Phys. Rev. B* **54**, 11169–11186 (1996).

36. G. Kresse, J. Furthmüller, Efficiency of ab-initio total energy calculations for metals and semiconductors using a plane-wave basis set. *Comp. Mater. Sci.* **6**, 15–50 (1996).

37. J. P. Perdew, K. Burke, M. Ernzerhof, Generalized gradient approximation made simple. *Phys. Rev. Lett.* **77**, 3865–3868 (1996).

38. P. E. Blöchl, Projector augmented-wave method. *Phys. Rev. B* **50**, 17953–17979 (1994).

39. G. Kresse, D. Joubert, From ultrasoft pseudopotentials to the projector augmented-wave method. *Phys. Rev. B* **59**, 1758–1775 (1999).

40. H. J. Monkhorst, J. D. Pack, Special points for Brillouin zone integrations. *Phys. Rev. B* **13**, 5188–5192 (1976).

41. K. Song, L. Liu, D. Zhang, M. P. Hautzinger, S. Jin, Y. Han, Atomic-resolution imaging of halide perovskites using electron microscopy. *Adv. Energy Mater.* **10**, 1904006 (2020).

42. A. De Backer, K. H. W. van den Bos, W. Van den Broek, J. Sijbers, S. V. Aert, StatSTEM: An efficient approach for accurate and precise model-based quantification of atomic resolution electron microscopy images. *Ultramicroscopy* **171**, 104–116 (2016).